Journal of Magnetism and Magnetic Materials 471 (2019) 359–364

Contents lists available at ScienceDirect

Journal of Magnetism and Magnetic Materials

journal homepage: www.elsevier.com/locate/jmmm

Research articles

First-order reversal curve (FORC) diagrams of nanomagnets with cubic magnetocrystalline anisotropy: A numerical approach

Miguel A. Valdez-Grijalva[a,b,*], Adrian R. Muxworthy[a]

[a] Department of Earth Science and Engineering, Imperial College London, SW7 2BP, UK
[b] Instituto Mexicano del Petróleo, 07730, Mexico

ARTICLE INFO

Keywords:
FORC diagram
Cubic magnetocrystalline anisotropy
Single-domain

ABSTRACT

First-order reversal curve (FORC) diagrams are increasingly used as a material's magnetic domain state fingerprint. FORC diagrams of noninteracting dispersions of single-domain (SD) particles with uniaxial magnetocrystalline anisotropy (MCA) are well studied. However, a large class of materials possess a cubic MCA, for which the FORC diagram properties of noninteracting SD particle dispersions are less understood. A coherent rotation model was implemented to study the FORC diagram properties of noninteracting ensembles of SD particles with positive and negative MCA constants. The pattern formation mechanism is identified and related to the irreversible events the individual particles undergo. Our results support the utility of FORC diagrams for the identification of noninteracting to weakly-interacting SD particles with cubic MCA.

1. Introduction

Ferromagnetic materials exhibit magnetic hysteresis: the dependence of the material's magnetisation $\boldsymbol{M}$ on its magnetic history [7]. The hysteretic response of a material is obtained by a series of measurements of its scalar magnetisation $M = \boldsymbol{M}\cdot\hat{\boldsymbol{n}}$ as a function of the applied magnetic field $\boldsymbol{H} = H\hat{\boldsymbol{n}}$. To trace a hysteresis loop the magnetic field strength H is slowly decreased from its saturation value $H = H_{\text{sat}}$ down to $H = -H_{\text{sat}}$, followed by the slow increase up to $H = H_{\text{sat}}$.

First-order reversal curves (FORCs) are a set of partial hysteresis curves, each starting at a saturation field $H = H_{\text{sat}}$, followed by the quasi-static decrease of the applied field strength down to $H = H_a$. From H_a, the field strength is increased back to $H = H_{\text{sat}}$ to trace a given curve labelled by its H_a value. On each FORC, the scalar magnetisation is then a function $M = M(H_b, H_a)$ of the applied field $H = H_b$ and the H_a value of the given curve ($H_a \leqslant H_b$). > The FORC distribution, an empirical analog of the Preisach weight function based on the experimental protocol described above, is defined as the second order mixed partial derivative [15]

$$\rho = \rho(H_b, H_a) = -\frac{1}{2}\frac{\partial^2 M}{\partial H_a \partial H_b}, \tag{1}$$

which must be understood in some weak sense to allow the discontinuous M. Contour plots of the FORC distribution (Eq. (1)) are known as FORC diagrams and have been increasingly used by the wide magnetics community as a proxy for the magnetic domain state and switching behaviour of a variety of magnetic systems [11,12,15,2,13].

Based on Stoner-Wohlfarth theory [16] significant progress has been made towards understanding the contribution of fine magnetic single-domain (SD) particles with uniaxial magnetocrystalline anisotropy (MCA) to the FORC diagram properties of interacting and non-interacting dispersions [10,4,2]. However, many materials including the most abundant ferromagnetic minerals on Earth possess a cubic MCA.

The general hysteretic properties of noninteracting dispersions of particles with cubic MCA has been previously studied [17,18]. The cubic MCA system is more complicated than the uniaxial due to the existence of more local energy minima (LEM) and the mechanism behind the FORC diagram pattern formation is not yet as well understood as the uniaxial case.

Previous studies of FORC diagram pattern formation by minerals with cubic MCA used micromagnetics [8] and dipole-dipole modelling [6] to study the influence of magnetostatic interactions on the FORC diagram. However, the fully non-interacting case remains less understood as these studies rely on specific arrangements of particle positions and orientations and focus only on magnetite-like materials.

In this study we present an approach for numerically calculating the FORC diagram of a uniform non-interacting dispersion of SD particles with cubic MCA. Since the properties depend linearly on the saturation magnetisation (M_S) and first anisotropy constant (K_1) (Section 2.1),

* Corresponding author at: Instituto Mexicano del Petróleo, 07730, Mexico.
E-mail address: mavaldez@imp.mx (M.A. Valdez-Grijalva).

https://doi.org/10.1016/j.jmmm.2018.09.086
Received 23 October 2017; Received in revised form 31 July 2018; Accepted 22 September 2018
Available online 25 September 2018

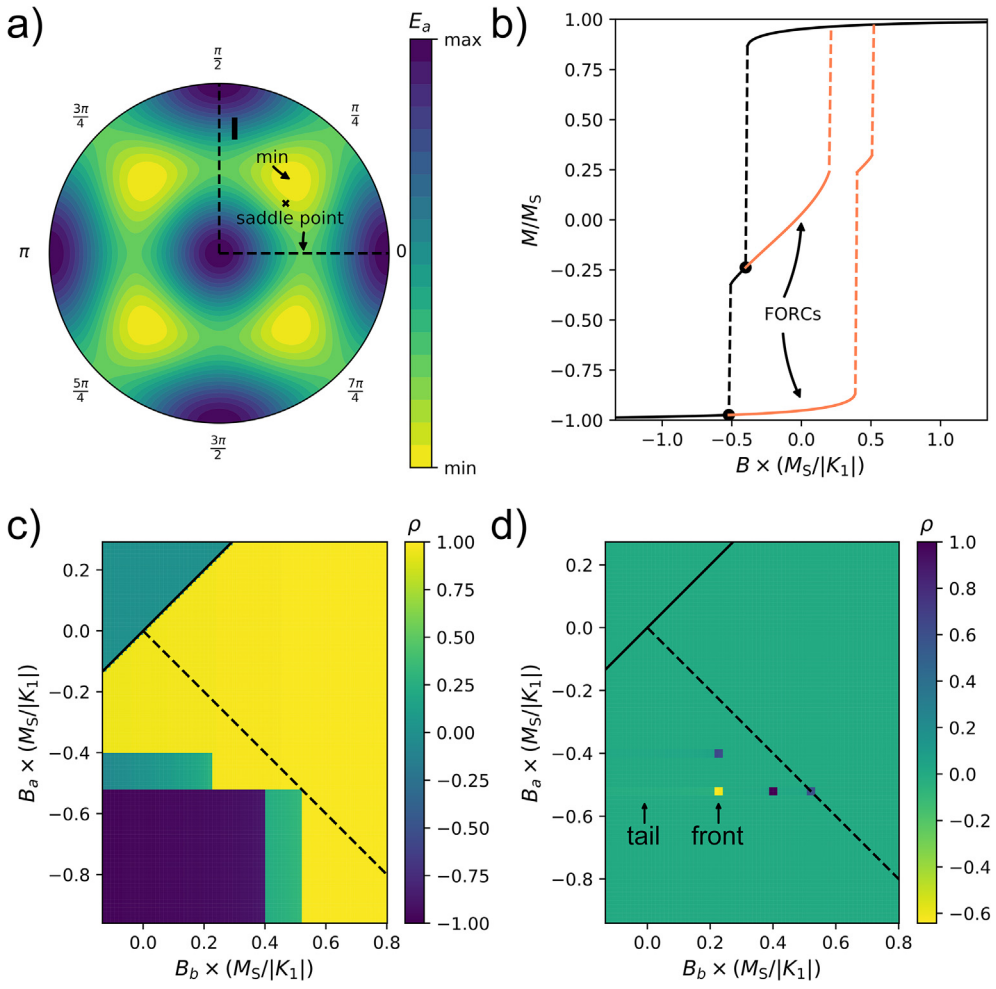

Fig. 1. Basic concepts: the single particle. a) Energy landscape projection in polar coordinates for $K_1 < 0$, $K_2 = 0$; b) a complete set of FORCs for θ, ϕ as marked by the $\times$ in a); c) the reduced magnetisation $m(B_b = \mu_0 H_b, B_a = \mu_0 H_a)$; d) the corresponding FORC distribution (normalised) with SF = 1. The FORC distribution fronts and tails coincide with the sharp edges of $m(B_b, B_a)$.

results obtained for a given set of parameters can be scaled to obtain the response for a different set of parameters. Thus, magnetic parameters of hypothetical iron-like ($K_1 > 0$) and magnetite-like ($K_1 < 0$) materials have been used due to their opposing signs for K_1. These are: iron-like, $M_s = 1 \times 10^5$ A/m and $K_1 = 1 \times 10^4$ J/m^3; magnetite-like, $M_s = 1 \times 10^5$ A/m and $K_1 = -1 \times 10^4$ J/m^3. This allows to obtain the FORC diagram for any set of parameters, whether with $K_1 > 0$ or $K_1 < 0$, by scaling operations.

2. Method

2.1. The FORC model

In an ensemble of identical, randomly aligned particles the probability of a given particle orientation is uniform over the sphere. If the ensemble is noninteracting (dilute) then the ensemble has a magnetic response

$$M{=}M(H_b, H_a) = \int_0^{2\pi}\int_0^{2\pi} m'(H_b, H_a, \theta, \phi)\sin\theta\, d\theta\, d\phi, \tag{2}$$

where $m'(H_b, H_a, \theta, \phi)$ is the magnetisation of a particle at (H_b, H_a) when the applied field is directed along the unit vector $\hat{\boldsymbol{n}} = \hat{\boldsymbol{e}}_r + \theta\hat{\boldsymbol{e}}_\theta + \phi\hat{\boldsymbol{e}}_\phi$. Given the symmetry of the cubic anisotropy system, the integration can instead be carried out over the subdomain $\mathbf{I} \equiv [0, \pi/2] \times [0, \pi/2]$, so:

$$M^{\dagger}{=}M^{\dagger}(H_b, H_a) = \frac{M(H_b, H_a)}{8} = \int_0^{\pi/2}\int_0^{\pi/2} m'(H_b, H_a, \theta, \phi)\sin\theta\, d\theta\, d\phi. \tag{3}$$

We calculate Eq. (3) using the backtracking line-search gradient method outlined in Section 2.2 to obtain each $m'(H_b, H_a, \theta, \phi)$ over a uniform grid $G \equiv \{i\pi/200{:}\ i = 0, ...,100\} \times \{j\pi/200{:}\ j = 0, ...,100\}$ with the evaluation performed in the center of the cells:

$$M^{*}{=}M^{*}(H_b, H_a) = \sum_i \sum_j m'(H_b, H_a, \theta_i, \phi_j)\sin\theta_i\, \Delta\theta\, \Delta\phi; \tag{4}$$

thus, 10^4 different particle/field configurations are simulated for.

The hysteresis loop of a single particle in the simplest case is a hysteron with switching fields H^- and H^+. In such a case, all the FORCs are contained in the main branches of the hysteresis loop (i.e., the field-descending and -ascending curves). The FORC distribution (Eq. (1)) is, accordingly:

$$\rho = -\frac{1}{2}\delta(H_a{-}H^-)\left\{\left[\frac{dm'}{dH_b}\right] + [m']\delta(H_b{-}H^+)\right\}, \tag{5}$$

where $[m']$ is, up to its sign, the size of the magnetisation discontinuity at the switching field H^+ and $[dm'/dH_b]$ the difference in the slopes between the main branches. The distribution has two parts: tail and front. The front contains the information about the magnetisation behaviour at the switching fields and has a delta-like support. The tail has

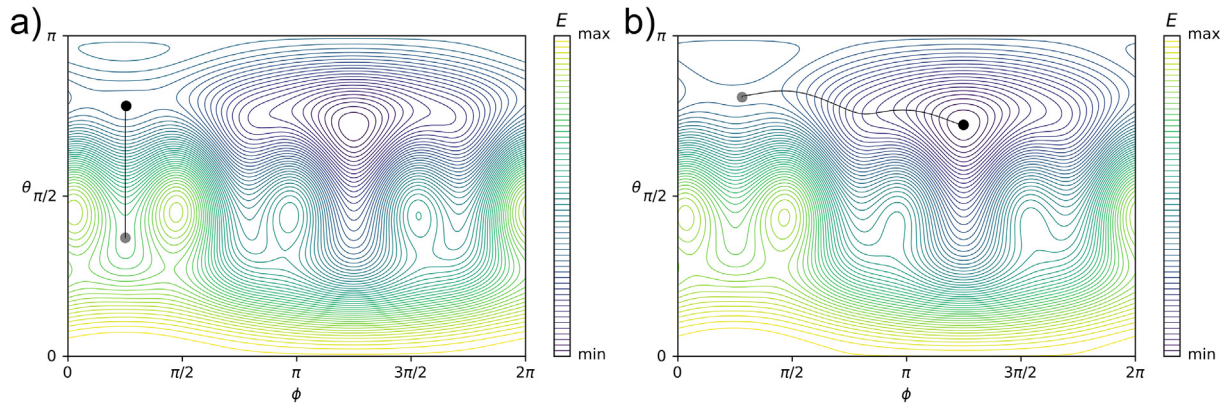

Fig. 2. The behaviour of the minimiser during irreversible motion along the main branch of the FORCs shown in Fig. 1b. a) The magnetisation irreversibly rotates from its position in the positive octant ($x, y, z > 0$) (grey dot) to the one with $z < 0$, where a local energy minimum is found (black dot). As the field strength is further increased the local energy minimum becomes more shallow until b) an energy gradient causes the irreversible motion to the negative octant ($x, y, z < 0$) where saturation occurs.

support along a line ($H_a = H^-, H_b < H^+$) and contains information about the slopes traced by the reversible motions. This contribution is usually an order of magnitude lower than the front so the reversible information is mostly obscured in a FORC diagram; however, using non-linear scales for the visualisation this contribution is highlighted.

For a single particle, the computation of the complete set of FORCs can be simplified if we note that each curve consists mostly of reversible motion with only a few irreversible jumps at the switching fields. This means that all the FORCs with H_a larger than the first switching field are implicitly calculated in the main branch of the hysteresis loop. Similarly for all the $m'(H_b, H_a)$ between the first (second) and second (third) switching fields, if there are more than one (two) irreversible jumps, and the $m'(B_b, B_a)$ between the last switching field and $-H_{\text{sat}}$. All that is left then, after calculating the hysteresis main branch, is to calculate the FORCs starting at H_a values corresponding to the switching fields (Fig. 1b). Once obtained, all $m'(H_b, H_a)$ form a grid m_i^j on which the FORC distribution can now be calculated (Fig. 1c). The calculation is done at each grid point by least-square fitting a second degree polynomial surface on a subgrid $\{m_{i+k}^{j+l}: k, l = -\text{SF}, \cdots, \text{SF}\}$, where SF is the so-called smoothing factor, taking care to exclude points with $H_b < H_a$; from the general equation of the fitted polynomial surface $m(H_b, H_a) = a_0 + a_1 H_a + a_2 H_b + a_3 H_a H_b + a_4 H_a^2 + a_5 H_b^2$ the FORC distribution is simply $-a_3/2$ [11].

In this study, the response of the randomly dispersed ensemble is obtained by simulating 10^4 different particle/field configurations and 5001 reversal curves calculated for each particle/field orientation.

2.2. Backtracking line-search gradient-descent method

A small spherical ferromagnetic particle in the single-domain (SD) state is modelled as a magnetic dipole with constant magnitude $|\boldsymbol{M}| = M_s$, the saturation magnetisation of the material. The magnetic Gibbs free-energy density of the particle is then the sum of the magnetocrystalline anisotropy (MCA) and the external field energy densities:

$$E = E_a + E_z \tag{6}$$

with

$$E_a = \frac{K_1}{2} \sum_{i \neq j} \alpha_i^2 \alpha_j^2 + K_2 \prod_i \alpha_i^2, \tag{7}$$

$$E_z = -M_s(\boldsymbol{m} \cdot \boldsymbol{B}) = -M_s B(\alpha\chi + \beta\psi + \gamma\omega); \tag{8}$$

where $\alpha_i = (\alpha, \beta, \gamma)$ are the direction cosines of the reduced magnetisation $\boldsymbol{m} = \boldsymbol{M}/|\boldsymbol{M}|$ and (χ, ψ, ω) those of the external field $\boldsymbol{B} = \mu_0 \boldsymbol{H}$;$K_1$ and K_2 the first and second MCA constants. From thermodynamics it is known that a system is spontaneously driven towards states with locally minimal Gibbs free-energy. Therefore, we are concerned with finding the LEM of the function $E = E(\boldsymbol{m}, \boldsymbol{B})$.

Since the reduced magnetisation vector is unitary, it is natural to express the energy in the spherical coordinate system $E = E(\boldsymbol{m} = \boldsymbol{m}(\theta, \phi), \boldsymbol{B})$ (θ, ϕ the polar and azimuthal angles, respectively):

$$E_a = K_1 \sin^2\theta [\cos^2\theta + (\sin\theta\cos\phi\sin\phi)^2] + K_2 \sin^2\theta (\sin\theta\cos\theta\sin\phi\cos\phi)^2, \tag{9}$$

$$E_z = -M_s B(\chi\sin\theta\cos\phi + \psi\sin\theta\sin\phi + \omega\cos\theta). \tag{10}$$

E_a minima and maxima lie along crystallographic orientations depending on the sign of K_1, K_2 and the ratio $|K_2|/|K_1|$. For $K_1 < 0$ ($K_2 = 0$) the easy axes (minima) are the ⟨1 1 1⟩ and the hard (maxima) the ⟨1 0 0⟩; the ⟨1 1 0⟩ are saddle points (Fig. 1(a)). When $K_1 > 0$ ($K_2 = 0$) instead, the easy axes become the ⟨1 0 0⟩ and the hard the ⟨1 1 1⟩ while the ⟨1 1 0⟩ remain as saddle points.

From Eq. (6), (9, 10), the gradient is then

$$\begin{aligned}\nabla E &= \hat{e}_\theta (E_a + E_z)_\theta + \hat{e}_\phi (E_a + E_z)_\phi \\ &= \hat{e}_\theta ((E_a)_\theta + (E_z)_\theta) + \hat{e}_\phi ((E_a)_\phi + (E_z)_\phi);\end{aligned} \tag{11}$$

where

$$\begin{aligned}(E_a)_\theta = 2\sin\theta\cos\theta \{ & K_1 [2(\sin\theta\sin\phi\cos\phi)^2 \\ & -\sin^2\theta + \cos^2\theta] \\ & + K_2 [2(\sin\theta\cos\theta\sin\phi\cos\phi)^2 - \sin^4\theta]\},\end{aligned} \tag{12}$$

$$(E_z)_\theta = -M_s B(\chi\cos\theta\cos\phi + \psi\cos\theta\sin\phi - \omega\sin\theta) \tag{13}$$

$$\begin{aligned}(E_a)_\phi = & 2\sin^4\theta\sin\phi\cos\phi (K_1 + K_2\cos^2\theta) \\ & \times (-\sin^2\phi + \cos^2\phi)\end{aligned} \tag{14}$$

$$(E_z)_\phi = -M_s B\sin\theta(-\chi\sin\phi + \psi\cos\phi). \tag{15}$$

A backtracking line-search gradient-descent method [1] was implemented to simulate hysteresis loops and first-order reversal curves of nanomagnets with cubic MCA. The Armijo-Goldstein control parameters $c = 1 \times 10^{-4}$, $\tau = 1/2$ were used in this study. These ensure that the minimiser follows the gradient-descent direction very closely (Fig. 2).

3. Results and discussion

The calculated FORCs for a single particle/field orientation are shown in Fig. 1(b). Fig. 1(c and d) show the magnetisation as a function of (B_b, B_a) and the corresponding FORC diagram (normalised, SF = 1),

respectively. It is seen that the distribution is a collection of tail/front pairs like Eq. (5) along the discontinuities in $m(B_b, B_a)$. A negative delta-like source at ($B_b = 0.23$, $B_a = -0.52$) (non-dimensional units) is caused by the curve with $B_a = -0.51$ going back to positive saturation at $B_b = 0.23$ while the one with $B_a = -0.52$ remains in its negative saturation state up to $B_b = 0.4$. These type of strong, highly-localised FORC distribution negative sources are then due to irreversible events on different FORCs. These strong, negative delta-like sources cannot occur in uniaxial particles which have only one irreversible event along the hysteresis main branch; low-valued negative delta-like sources are possible in uniaxial systems for the particles with easy axis almost normal to the applied field which experience very small irreversible upward jumps [16,10].

The particles that have an easy axis alignment closer to the external field produce highly-symmetric, hysteron-like hysteresis curves which are responsible for the accumulation of positive delta-like sources along the central ridge (the line $H_a = -H_b$). Materials with $K_1 > 0$ have higher intrinsic (i.e. non-dimensional) coercivities. The highest coercivity B_C was found to be as high as ~ 1.5 for particles with an easy axis closely aligned with the applied field. For $K_1 < 0$ the coercivities are as high as ~ 1. The lowest coercivities are ~ 0.75 and ~ 0.35 for positive and negative K_1, respectively.

FORC diagrams are usually presented as contour plots of the FORC distribution with higher values of the smoothing factor. The usual plotting axes are the transformed $B_c = (B_b - B_a)/2$, $B_u = (B_b + B_a)/2$; in this manner, FORC diagrams were calculated (Figs. 3, 4). The FORC distributions show similar, yet different, patterns for both signs of K_1 (Figs. 3, 4). In the $K_1 < 0$ case, positive delta-like sources accumulate along the central ridge from ~ 0.35 up to ~ 1 (Fig. 4). A local peak (Fig. 4, region ii) is caused by a cascade of particles with easy axis far from the field orientation switching at low B_a values to intermediate states and back to positive saturation at $B_b < |B_a|$. These irreversible events then cause the accumulation of negative delta-like sources along a negative-valued vertical ridge (Fig. 4, region i). To the right of this, negative contributions produced by the irreversible events of particles undergoing hysteresis loops with more than two jumps, which corresponds to the fraction of particles with hard axes very closely aligned with the external field, cause the structure of region iii to differ significantly from the $K_1 > 0$ case (Fig. 3, region iii).

For $K_1 > 0$ (Fig. 3), the pattern formation is similar, if only with the position and width of the features changing. However, a fundamental difference is that for $K_1 > 0$ there is not an appreciable fraction of particles with hysteresis loops with more than two irreversible events. This is manifested in the FORC distribution by the absence of negative sources to the right of the negative vertical ridge as well as by diminished positive contributions, which causes the boomerang-shaped feature (Fig. 3, region iii).

The position of the features in the FORC diagram for $K_1 < 0$ (Fig. 4) is slightly offset from being centered around the $B_u = 0$ axis. This has been observed before in both measured and modelled FORC diagrams [6,8–10]. Newell [10] attributes this to either a numerical artifact introduced by the least-square fitting-type calculation of the FORC distribution or to thermal effects. However, at least in this study, this should be attributed to the irreversible contributions accumulating just below the central ridge, which are absent in the $K_1 > 0$ case.

The FORC diagrams obtained here for non-interacting ensembles of SD particles with cubic MCA show good agreement with the weakly interacting ensembles of Harrison and Lascu [6] as far as overall shape, e.g., the tilted negative ridge (Figs. 3, 4). The elongated, negative-valued ridge is highly significant and related to the presence of intermediate states, i.e., more than one irreversible event along the hysteresis curve. Uniaxial particles cannot produce this type of FORC distribution sources [8,10], so this is possibly a unique magnetic fingerprint of non-interacting to weakly interacting, coherent-rotating SD particles with cubic MCA or other non-uniaxial types of MCA. The tilted negative ridge has been observed before in FORC measurements of synthetic and natural greigite ($K_1 < 0$ [19]) samples [14].

For comparison with Harrison and Lascu [6], FORC diagrams for materials with log-normal distributions of K_1 were produced for both signs of K_1. The probability density function

$$W(K^*) = \frac{1}{K^*\sigma\sqrt{2\pi}}\exp\left(-\frac{1}{2}\left(\frac{\log K^* - \mu}{\sigma}\right)^2\right), \tag{16}$$

where $K^* = K/K1$, with $\mu = -1/32$ and $\sigma = 1/4$ was used for calculating the weighted averages, e.g., for a K value twice the material's value for K_1 the weight factor is equal to $W(2)$. Values of M_S, K_1 for iron and magnetite were used: for iron, $M_s = 1.7 \times 10^6$ A/m [3] and $K_1 = 4.8 \times 10^4$ J/m^3 [5]; for magnetite, $M_s = 4.8 \times 10^5$ A/m and $K_1 = -1.2 \times 10^4$ J/m^3 [3]. The FORC diagram for magnetite (Fig. 5b) is remarkably similar to that by Harrison and Lascu [6]. The difference between both K_1 sign cases is most apparent when comparing the negative ridge shapes (Fig. 5, regions i) and the shape of the boomerang region (Fig. 5, regions iii). The range of coercivities (Fig. 5, insets) was found to be 10–50 mT for iron and 5–30 mT for magnetite, with a peak response at ~ 22 mT and ~ 12 mT, respectively. These peak responses are relatively large compared to rock magnetic measurements, namely 5–15 mT for iron and 3–12 mT for magnetite [3]. This is due to our model not incorporating thermal switchings and having a broad

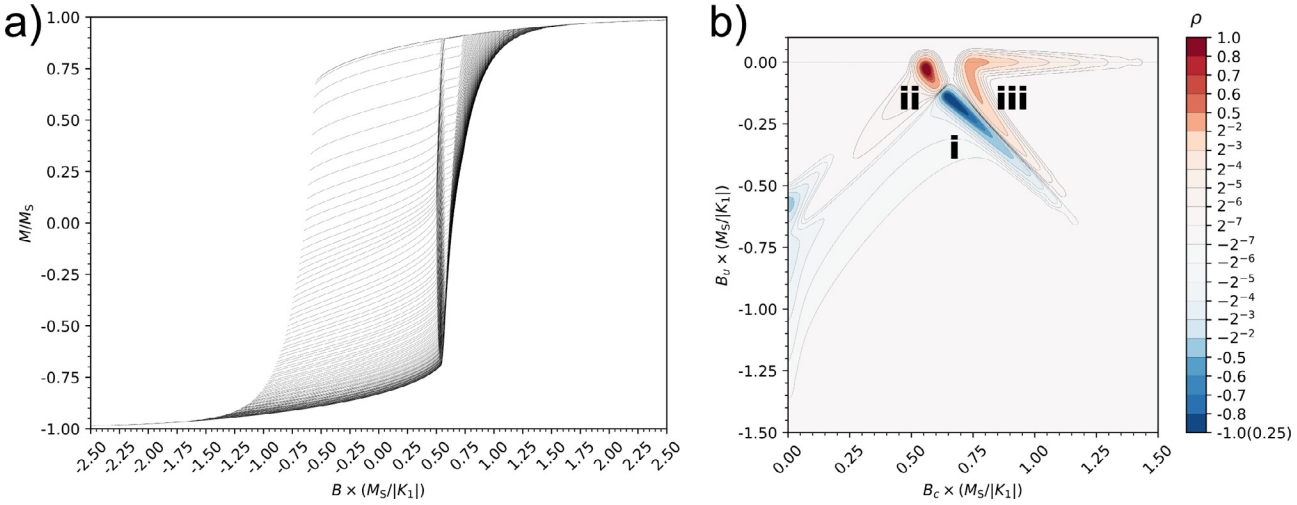

Fig. 3. Reversal curves and FORC diagram for $K_1 > 0$. a) Reversal curves (every tenth curve is shown) and b) corresponding FORC diagram (SF = 10). Gaussian filtering was used for further smoothing.

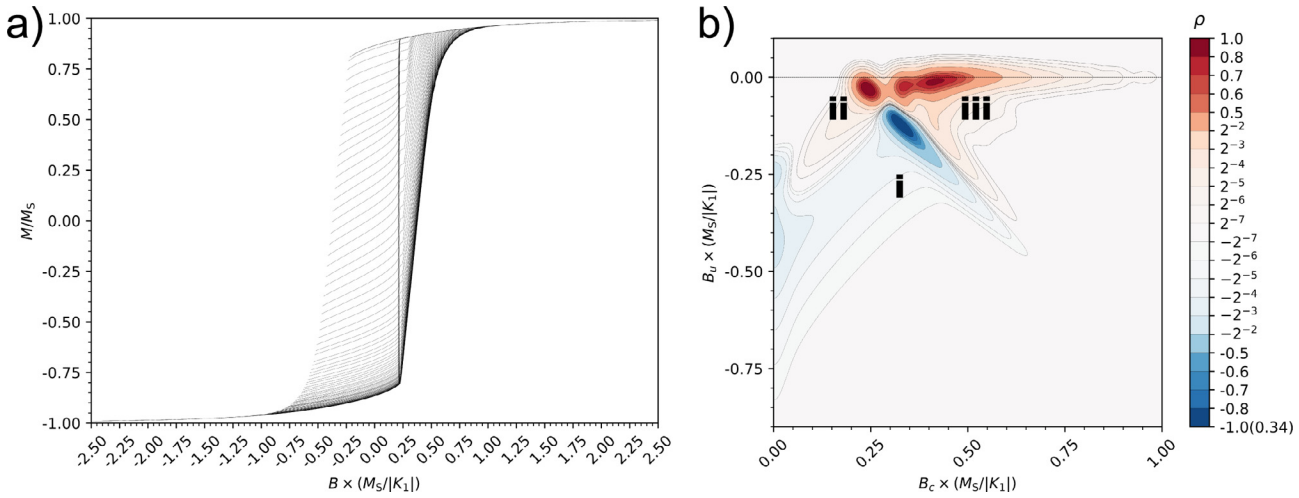

Fig. 4. Reversal curves and FORC diagram for $K_1 < 0$. a) Reversal curves (every tenth curve is shown) and b) corresponding FORC diagram (SF = 10). Gaussian filtering was used for further smoothing.

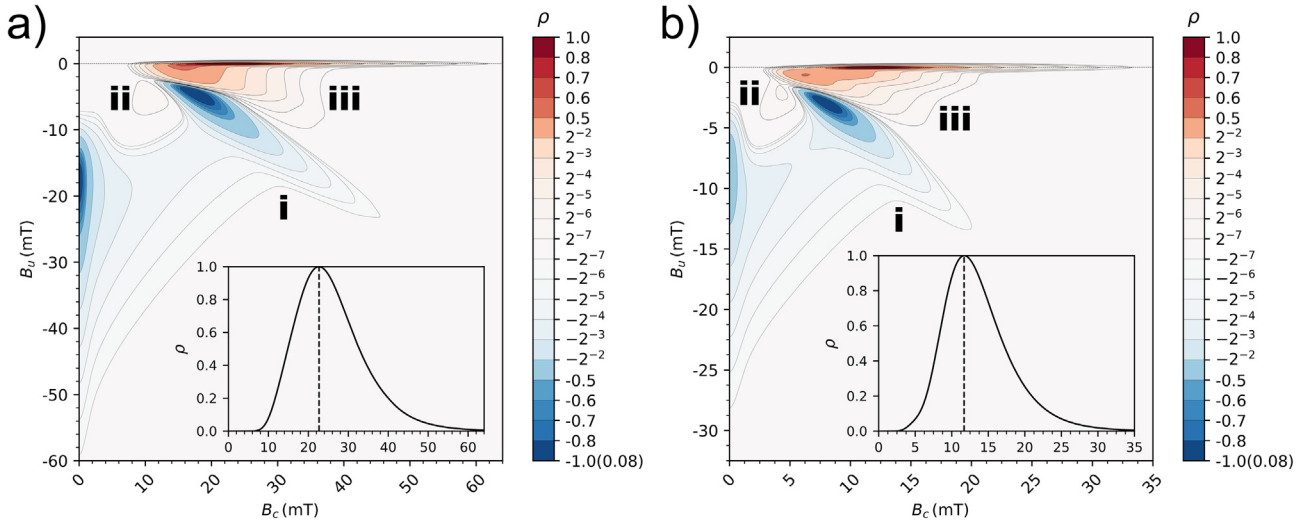

Fig. 5. FORC diagrams for log-normal distributions of K_1. a) Iron ($K_1 > 0$); b) magnetite ($K_1 < 0$). The patterns are similar in overall shape, yet show some differences, more markedly in regions i and iii. Inset: ρ along the $B_u = 0$ axis (central ridge).

distribution of K_1 values.

4. Conclusion

The FORC distribution and diagram of noninteracting dispersions of SD particles with cubic MCA was calculated. The numerical algorithm was found to be robust and fast. It is important that the minimiser takes sensible steps in order to closely follow the gradient-descent direction and not end up in local energy minima across energy barriers; the Armijo-Goldstein control parameters used in this study ensure these conditions.

The mechanism behind the FORC diagram pattern formation of dilute dispersions of SD particles with cubic MCA was identified. Different patterns emerge according to the sign of K_1. The main difference between the $K_1 < 0$ and $K_1 > 0$ cases is that for the negative case there are more particles in the randomly aligned ensemble which support up to two intermediate states during hysteresis. This in turn causes the regions labelled iii (Figs. 3–5)) to take on distinct shapes. The FORC diagram pattern of non-interacting to weakly interacting, cubic MCA SD particle ensembles are robust, which supports the idea of FORC diagram use for the identification of a noninteracting to weakly-interacting fraction of SD particles with cubic MCA.

The elongated negative ridge can be interpreted as the FORC signal unique to noninteracting to weakly-interacting SD particles with cubic or other non-uniaxial types of MCA. Identification of this signal should be straightforward since its noninteracting nature means that it is essentially additive. Experimental work with dilute dispersions of fine particles of iron, magnetite or other magnetic minerals with a cubic MCA can provide confirmation.

Acknowledgments

This research was supported by Instituto Mexicano del Petróleo scholarship PCTRES (MAVG) as well as by NERC grant NE/J020508/1 (ARM).

References

[1] L. Armijo, Minimization of functions having Lipschitz continuous first partial derivatives, Pac. J. Math. 16 (1) (1966) 1–3, https://doi.org/10.2140/pjm.1966.16.1.
[2] E. De Biasi, J. Curiale, R.D. Zysler, Quantitative study of FORC diagrams in thermally corrected Stoner-Wohlfarth nanoparticles systems, J. Magn. Magn. Mater. 419 (2016) 580–587, https://doi.org/10.1016/j.jmmm.2016.06.075.
[3] D.J. Dunlop, Ö. Özdemir, Rock Magnetism, Cambridge University Press, Cambridge, 1997.
[4] R. Egli, A.P. Chen, M. Winklhofer, K.P. Kodama, C.S. Horng, Detection of

noninteracting single domain particles using first-order reversal curve diagrams, Geochem. Geophys. Geosyst. 11 (1) (2010), https://doi.org/10.1029/2009GC002916.
[5] C.D. Graham Jr., Magnetocrystalline anisotropy constants of iron at room temperature and below, Phys. Rev. 112 (4) (1958) 1117, https://doi.org/10.1103/PhysRev. 112.1117.
[6] R.J. Harrison, I. Lascu, Forculator: a micromagnetic tool for simulating first-order reversal curve diagrams, Geochem. Geophys. Geosyst. 15 (12) (2014) 4671–4691, https://doi.org/10.1002/2014GC005582.
[7] I. Mayergoyz, Mathematical models of hysteresis, IEEE Trans. Magn. 22 (5) (1986) 603–608, https://doi.org/10.1109/TMAG.1986.1064347.
[8] A.R. Muxworthy, D. Heslop, W. Williams, Influence of magnetostatic interactions on first-order-reversal-curve (FORC) diagrams: a micromagnetic approach, Geophys. J. Int. 158 (3) (2004) 888–897, https://doi.org/10.1111/j.1365-246X.2004.02358.x.
[9] A.R. Muxworthy, J.G. King, D. Heslop, Assessing the ability of first-order reversal curve (FORC) diagrams to unravel complex magnetic signals, J. Geophys. Res. (B1) (2005) 110, https://doi.org/10.1029/2004jb003195.
[10] A.J. Newell, A high-precision model of first-order reversal curve (FORC) functions for single-domain ferromagnets with uniaxial anisotropy, Geochem. Geophys. Geosyst. 6 (5) (2005), https://doi.org/10.1029/2004GC000877.
[11] C.R. Pike, A.P. Roberts, K.L. Verosub, Characterizing interactions in fine magnetic particle systems using first order reversal curves, J. Appl. Phys. 85 (9) (1999) 6660–6667, https://doi.org/10.1063/1.370176.
[12] C.R. Pike, C.A. Ross, R.T. Scalettar, G. Zimanyi, First-order reversal curve diagram analysis of a perpendicular nickel nanopillar array, Phys. Rev. B 71 (13) (2005) 134407, https://doi.org/10.1103/PhysRevB.71.134407.
[13] M.P. Proenca, C.T. Sousa, J. Ventura, J. Garcia, M. Vazquez, J.P. Araujo, Identifying weakly-interacting single domain states in Ni nanowire arrays by FORC, J. Alloy. Compd. 699 (C) (2017) 421–429, https://doi.org/10.1016/j.jallcom.2016.12.340.
[14] A.P. Roberts, L. Chang, C.J. Rowan, C.S. Horng, F. Florindo, Magnetic properties of sedimentary greigite (Fe_3S_4): an update, Rev. Geophys. 49 (1) (2011), https://doi.org/10.1029/2010RG000336.
[15] A.P. Roberts, C.R. Pike, K.L. Verosub, First-order reversal curve diagrams: a new tool for characterizing the magnetic properties of natural samples, J. Geophys. Res. 105 (B12) (2000) 28461–28475, https://doi.org/10.1029/2000JB900326.
[16] E.C. Stoner, E.P. Wohlfarth, A mechanism of magnetic hysteresis in heterogeneous alloys, Philos. Trans. R. Soc. A 240 (826) (1948) 599–642 URLhttps://www.jstor.org/stable/91421.
[17] N.A. Usov, S.E. Peschany, Theoretical hysteresis loops for single-domain particles with cubic anisotropy, J. Magn. Magn. Mater. 174 (3) (1997) 247–260, https://doi.org/10.1016/S0304-8853(97)00180-7.
[18] M. Walker, P. Mayo, K. O'Grady, S. Charles, R. Chantrell, The magnetic properties of single-domain particles with cubic anisotropy. I. Hysteresis loops, J. Phys.: Condens. Matter 5 (17) (1993) 2779, https://doi.org/10.1088/0953-8984/5/17/012.
[19] M. Winklhofer, L. Chang, S.H.K. Eder, On the magnetocrystalline anisotropy of greigite (Fe_3S_4), Geochem. Geophys. Geosyst. 15 (4) (2014) 1558–1579, https://doi.org/10.1002/2013GC005121.